



Swansea University
Prifysgol Abertawe



Cronfa - Swansea University Open Access Repository

This is an author produced version of a paper published in :
Materials Science and Engineering: A

Cronfa URL for this paper:

<http://cronfa.swan.ac.uk/Record/cronfa25184>

Paper:

Buckingham, R., Argyrakis, C., Hardy, M. & Biroasca, S. (in press). The Effect of Strain Distribution on Microstructural Developments during Forging in a Newly Developed Nickel Base Superalloy. *Materials Science and Engineering: A*

<http://dx.doi.org/10.1016/j.msea.2015.12.042>

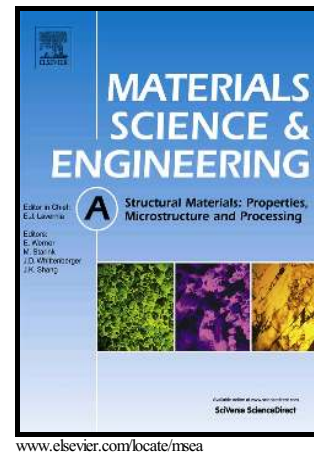
This article is brought to you by Swansea University. Any person downloading material is agreeing to abide by the terms of the repository licence. Authors are personally responsible for adhering to publisher restrictions or conditions. When uploading content they are required to comply with their publisher agreement and the SHERPA RoMEO database to judge whether or not it is copyright safe to add this version of the paper to this repository.

<http://www.swansea.ac.uk/iss/researchsupport/cronfa-support/>

Author's Accepted Manuscript

The Effect of Strain Distribution on Microstructural Developments during Forging in a Newly Developed Nickel Base Superalloy

R.C. Buckingham, C. Argyrakis, M.C. Hardy, S. Biroasca



PII: S0921-5093(15)30733-4
DOI: <http://dx.doi.org/10.1016/j.msea.2015.12.042>
Reference: MSA33125

To appear in: *Materials Science & Engineering A*

Received date: 15 September 2015
Revised date: 12 December 2015
Accepted date: 14 December 2015

Cite this article as: R.C. Buckingham, C. Argyrakis, M.C. Hardy and S. Biroasca
The Effect of Strain Distribution on Microstructural Developments during
Forging in a Newly Developed Nickel Base Superalloy, *Materials Science &
Engineering A*, <http://dx.doi.org/10.1016/j.msea.2015.12.042>

This is a PDF file of an unedited manuscript that has been accepted for publication. As a service to our customers we are providing this early version of the manuscript. The manuscript will undergo copyediting, typesetting, and review of the resulting galley proof before it is published in its final citable form. Please note that during the production process errors may be discovered which could affect the content, and all legal disclaimers that apply to the journal pertain

The Effect of Strain Distribution on Microstructural Developments during Forging in a Newly Developed Nickel Base Superalloy

R.C. Buckingham^a, C. Argyrakis^b, M.C. Hardy^b and S. Biroasca^a

^aInstitute of Structural Materials, Swansea University, Bay Campus, Fabian Way, Swansea, SA1 8EN, UK.

Email: 522042@swansea.ac.uk; ross_c_b@hotmail.com, Mobile number: +44 (0) 7890667206; Tel. number: +44 (0) 1792606437 (Dr. Soran Biroasca)

^bRolls-Royce plc, PO Box 31, Derby, DE24 8BJ, UK.

Abstract

In the current study, the effect of strain distribution in a simple forging geometry on the propensity for recrystallisation, and its impact on mechanical properties has been investigated in a newly developed experimental nickel-based superalloy. The new alloy was produced via a Powder Metallurgy (PM) route and was subsequently Hot Isostatic Processed (HIP), isothermally forged, and heat treated to produce a coarse grain microstructure with average grain size of 23-32 μm . The alloy was examined by means of Electron Back-Scatter Diffraction (EBSD) to characterise the microstructural features such as grain orientation and morphology, grain boundary characteristics and the identification of potential Prior Particle Boundaries (PPBs) throughout each stage of the processing route. Results at the central region of the cross-section plane parallel to the loading direction showed significant microstructural differences across the forging depth. This microstructural variation was found to be highly dependent on the value of local strain imparted during forging such that areas of low effective strain showed partial recrystallisation and a necklace grain structure was observed following heat treatment. Meanwhile, a fully recrystallised microstructure with no PPBs was observed in the areas of high strain values, in the central region of the forging.

Keywords:

Nickel-based superalloy, Forging, Recrystallization, Microstructure, EBSD.

1. Introduction

Nickel-based superalloys are a class of alloys which exhibit exceptional mechanical properties and reliable corrosion resistance at high temperatures. It is for this reason they are predominantly used in the aerospace industry, especially in the hot rotational sections of the gas turbine. With the increasing requirement for fewer emissions within the aviation industry, aero engine manufacturers are pushing for more efficient gas turbine engines capable of operating at higher temperatures. The high temperature performance of polycrystalline nickel-based superalloys can be accredited to a combination of solid solution strengthening within the Al γ matrix and the precipitation of an ordered L1₂ γ' phase. The strength attributed to γ' is dependent on the size and distribution of the precipitates within the microstructure where typically higher temperature capability requires an increase in the volume fraction of γ' . This can be achieved by increased concentrations of precipitate forming elements such as Al, Ti, Ta and Nb [1,2], although excessive amounts of Ti, Ta and Nb can lead to precipitation of η phase, which is undesirable. However, with increased quantities of elements that partition to γ' , there is a greater risk of forming Topologically Close Packed (TCP) phases during high temperature exposure. Particularly if high levels of refractory metals, notably Mo and W, are also added to strengthen the γ phase and high levels of Cr are maintained for resistance to hot corrosion and oxidation.

Powder Metallurgy (PM) processing is often the preferred method of producing material for large, thick section components in compositions that show high volume fractions of γ'

precipitates and refractory metals due to the potential for significant segregation from traditional ingot metallurgy. [3,4]. The benefits of PM processing are the result of high rates of solidification in freezing small molten droplets, which reduces levels of segregation to a micro length scale in powder particles. Hot Isostatic Pressing (HIP) is used to consolidate the powder in steel containers at high pressures and temperatures to create a fully densified compact. It is desirable for critical engineering applications to subsequently hot work compacted powder to improve material properties by refining grain size and disrupting the network of carbides, oxides and oxy-carbides, known as Prior Particle Boundaries (PPBs). The PPBs form on the surface of powder as a consequence of oxygen and elemental segregation from the powder and from migration and spheroidising of C during the HIPing process. Details of the PM and Thermo-Mechanical Processing (TMP) route can be found in the literature [5], and has been used to create several nickel based superalloys for use in gas turbines, including RR1000 [6,7]. The parameters chosen throughout TMP, particularly the HIP, forging and heat treatment processes are critical in defining the final microstructure. It is therefore vital to observe the development of microstructure for the alloy during TMP and to understand the exact mechanisms of recovery and recrystallisation that occur during processing in order to achieve a homogenous microstructure. Further related aspects of the effect of varying processing parameters and thermal treatments has been previously reported in [8].

Successful hot working of high γ' containing nickel-based superalloys requires high temperatures and low strain rates to promote superplasticity and avoid loss of ductility, which gives rise to cracking from lower temperature and higher strain rate deformation. As such, isothermal conditions are necessary to maintain high temperatures over relatively long periods of time to impose low strain rates. It is believed that during the isothermal forging of nickel-based alloys, recovery and dynamic recrystallisation compete and the dominance is

dependent on the forging temperature, strain rate and level of reduction [9,10]. More importantly, the occurrence of dynamic recrystallisation has been proven to have a significant role in grain refinement and material softening during forging which can aid to improve workability and mechanical properties [11] through the generation of high angle grain boundaries [12]. It is not clear from the literature which mechanism dominates in nickel-based superalloys, however, it is well established that dynamic recrystallisation is dominating at low temperatures and high strain rates [10,13] where nucleation occurs as a result of strain induced grain boundary migration [9]. The mechanism of grain boundary migration during static recrystallisation is similar to that in dynamic recrystallisation; however it occurs during static thermal heat treatments at temperatures between 0.5 and 0.8 of the melting temperature of the alloy. It is reported that during static recrystallisation, the levels of strain accumulation within the microstructure during the processing can have a marked effect on the rate at which new grains nucleate and grow to consume the material previously undergoing dynamic recrystallisation processes [10]. Furthermore, the twin boundary formation and growth in FCC systems and its correlation with microstructure modification, particularly post dynamic recrystallisation, should be considered during hot deformation processes and subsequent heat treatment. Although the formation of twin boundaries are not well understood, several postulations are suggested in literature including via formation from packets of stacking faults as a result of grain boundary migration [14 – 16], or high angle grain boundary dissociation into a coherent twin boundary, an incoherent twin boundary and low energy boundary [14,17,18]. Moreover, it is well reported that a high number of twin boundaries can enhance the mechanical property and corrosion resistance in many alloy systems including steel, nickel and copper [19 – 21]. This aspect is particularly important for nickel-based superalloys used in aero-engines as a method of improving corrosion and fatigue resistance

through increasing twins volume fraction without alteration of the alloy's chemical composition [22][23].

In the current study, forging of an advanced nickel-based (PM) prepared superalloy is investigated using computational process modelling to predict the strain distribution in a forged condition followed by characterisation of microstructure and microtexture using Electron Back-Scatter Diffraction (EBSD). Moreover, EBSD was utilised to aid in understanding the evolution of material microstructure throughout the forging process in both as-forged and heat treated conditions. A correlation is made between the effects of strain variation across an isothermally forged specimen on the propensity for recrystallisation, grain growth and twin boundary formation and hence their impact on mechanical properties is discussed.

2. Materials and Experimental Procedures

2.1 Materials Used

The study uses a newly developed experimental nickel-based superalloy V207M with a nominal chemical composition by weight% of 19-Cr, 4-Co, 9-Fe, 0.35-Mo, 0.9-W, 5.5-Al, 3.5-Nb, 0.7-Ta, 1.0-Ti, 0.15-C, 0.15-B, 0.035-Zr and balance nickel [24]. Initial powder production was conducted at Allegheny Technologies Incorporated (ATI) Powder Metals in Pittsburgh, USA. The powder was produced via argon gas atomisation which was sieved through screens to obtain a maximum particle size of 53 μm . The powder was filled into a mild steel container, de-gased and sealed, and HIP consolidated under vacuum at a pressure of 100 MPa and a temperature lower than the γ' solvus temperature. Two as-HIP compacts were machined to a height of 76 mm and diameter of at least 65mm and isothermally forged at a temperature of 1050°C and upset rate of 0.2 mm/mm/min, in-line with the findings in [8],

at ATI Forged Products, Cudahy, USA. Both forgings were left to cool in air following compression and removal from the forging chamber. One forging was kept in the as-forged condition whilst the second underwent a solution (1120°C/2 hrs) and age (850°C/4 hrs) heat treatment to allow for static recrystallisation and grain growth to an average grain size of 23-32 μm diameter (ASTM 6-7) at the centre of the forging. The process parameters were chosen based on earlier research where forging temperature and upset rate were adequate to produce a partially recrystallised microstructure.

2.2 Sample Preparation and EBSD Data Collection

Both forging blanks were sectioned along their centre to reveal a plane perpendicular to the forging axis in correspondence with the computational model used in this study. Figure 1 schematically shows the forging section with the area of interest highlighted. Care was taken during sectioning to minimise levels of deformation imparted on the plane of interest. The sectioned material was mounted in conductive Bakelite and prepared following standard grinding and polishing procedures prior to final 0.04 μm colloidal silica polishing for a period of 15 minutes. EBSD examination was carried out on a Phillips XL30 tungsten filament Scanning Electron Microscope (SEM) equipped with Oxford Instruments HKL Channel 5 data acquisition and analysis software. An operating voltage of 20 kV was used to optimise the diffraction patterns of nickel. In total 16 equally spaced EBSD scans were performed on the material cross section for each forging blank. All EBSD scans were conducted along the vertical centreline of the forging parallel to the forging direction at an effective radius of zero. The step size remained consistent throughout each scan and was chosen in line with common EBSD methodology. For the two forgings investigated an indexing rate of at least 95% was achieved. Following completion of data acquisition, each area was analysed for grain size,

grain boundary characteristics and texture with grain size analysis conducted in accordance with ASTM E2627-13 and excluded twin boundaries.

2.3 Analysis of Powder and As-HIPed Material

To build a complete understanding of the microstructural evolution, SEM and EBSD examination was conducted on the alloy powder as well as in as-HIPed form. For examination of the as-HIPed material, a small section was removed from the consolidated cylinder prior to isothermal forging and mounted in Bakelite. The specimen was prepared by the same means as the forged material for EBSD data acquisition. To aid in imaging of Prior Particle Boundaries (PPB), the specimen was subsequently electro-etched using 10% orthophosphoric acid for 3-5 seconds to remove the γ matrix.

2.4 Process Modelling of Isothermal Forging

The forging process was modelled using Finite Element Method (FEM) software Deform2D simulation package developed by Scientific Forming Technologies Corporation, Ohio/USA. The software is tailored to deformation processes and is widely used in industry as a tool to simulate various manufacturing processes. It allowed for the prediction of strain levels and its distribution along the forging direction as well as the level of friction and thus adiabatic heating throughout the forging. To simulate the alloy accurately, the model used material properties accumulated through previous research on the alloy and assumed isothermal conditions throughout compression. Further information about the software and required parameters can be obtained through the developers online resources [25].

3. Results and Discussion

3.1 Process Modelling and Strain Mapping

Figure 2 presents the visual representation of the strain distribution and the variation of strain throughout the forging blank at two circumferential radii. The results of the process modelling indicated a symmetrical variance about the radial centreline of the forging, as well as circumferentially symmetrical about the forging axis, as is expected. In order to make a comparison, data was captured at the centre of the forging parallel to the compression axis and at a radial distance of 20mm. Comparison of the data revealed the maximum variance in effective strain was seen along the forging axis at a radius of 0mm (the centre of the forging), where the lowest levels of strain were seen close to the surface, gradually increasing to a maximum at the forging centre where levels of deformation are greatest. With increasing radial distance from the forging centre, the range in effective strain decreased with a 48% increase in effective strain at the surface by a radius of 20mm. The comparison was useful in understanding the effective size and shape of the 'dead zone' which can vary depending on forging parameters. Typically the 'dead zone' manifests as a cone or hemisphere which is visually observable in Figure 2(a) within which the levels of deformation are at a minimum. Under such a condition this area might contain a higher volume fraction of PPBs and thus produce an inhomogeneous microstructure. At the centre of the forging, the variation in effective strain with increasing radius is considerably less with a 3.9% increase in effective strain at the centre when compared to that seen at a distance of 20 mm, see Figures 2(a) and 2(b).

Examination of predicted levels of adiabatic heating indicate a maximum increase in temperature within the centre of the forging as is typical for forging process. Whereas, close to the surface a small increase of $\approx 1.4^{\circ}\text{C}$ is predicted with a maximum temperature increase

of $\approx 2.8^\circ\text{C}$ at the centre. From available literature, it is suggested that the majority of mechanical work during compression is converted to heat [26] but the results of the process modelling suggests the slow upset rate has minimised the adiabatic heating affect. Understanding adiabatic heating is initially of great interest when investigating the parameters for conventional press forging as it can cause decreases in flow stresses as a result of softening [27] and trigger dynamic processes such as recrystallisation. It should be noted that the greatest effect is seen at moderate to high strain rates and is assumed to be insignificant at the slow strain rates required to achieve superplastic forming. The results in the current study follow this assumption where the levels of temperature increase were insignificant as a result of the slow strain rate. It was therefore considered negligible when considering its effect on dynamic recrystallisation and recovery during forging processes.

3.2 Examination of Powder and As-HIPed Material

Figure 3 presents alloy V207M in as-received alloy powder. From the secondary electron image the particle size distribution is seen to support previous research conducted on similar powder alloy which found $>90\%$ of the powder was smaller than $38\mu\text{m}$ [28]. Examination of the powder in Figure 3(a) shows both satellite particles (highlighted by vertical arrows) and melt impacts (highlighted by horizontal arrows), as is commonly seen in powder metallurgy produced via gas atomisation.

The presence of PPB was microscopically investigated as shown in Figure 3 (b). Clearly observable from the image is the appearance of a PPB around a powder particle, and is in agreement with previous study [8]. It is this network of PPBs within the final microstructure that can be detrimental to the mechanical property of the alloy. Also observable from Figure 3 (b) is the presence of a needle-like δ phase. It should be noted that most of the needle-like δ -phase was found to go into solution on forging resulting in no δ -phase in the final

microstructure. The absence of the intermetallic δ -phase after forging was also reported in [8]. Figure 4 shows the microstructure and texture of the as-HIPed alloy. The Inverse Pole Figure (IPF) map in Figure 4(a) shows a clear presence of spherical grain boundaries with a bimodal distribution of the grain size and an average grain size of 4 μm . The IPF map in Figure 4(a) and Orientation Distribution Function (ODF) plots in Figure 4(b) (expressed in multiples of uniform density, m.u.d.) show very weak texture with a maximum intensity of only 2.26 m.u.d., as would be expected from the isostatic consolidation process.

3.2 The Effective Strain Effects on Microstructural Development during Forging

The IPFs and ODFs in Figure 5 show the microstructure and texture of the forged material at the surface, quarter depth and centre of the forging in A, B and C, respectively. It should be noted that only 3 maps out of the 16 EBSD maps are shown here. From the IPF maps the increase in grain size is evident with increasing depth and strain. Moreover, a presence of spherically shaped grains close to the surface is also observed. The number of these spherical grains is seen to decrease with depth where the grain size distribution becomes much more homogeneous at the centre of the forging. Average grain size data from all of the 16 EBSD maps are shown in Figure 6 with increasing distance from the surface. The graph supports the IPF maps in showing increased coarsening occurrence from the surface to the centre of the forging blank. Although the grain growth variation between surface and centre of the forged materials is relatively small ($<1\mu\text{m}$), the small level of grain coarsening is indicative of dynamic recrystallisation during the forging process. Furthermore, the occurrence of dynamic recrystallisation is evident from grain size differences between as-HIPed and as-forged materials shown by the IPFs in Figures 4 and 5. This is also indicated by the texture changes from random in as-HIPed to higher volume fractions of Cube (001) $\langle 100 \rangle$, Rotated Cube

(001)<110> and Goss (110)<001> texture components in as-forged material, shown by the ODFs in Figures 4 and 5.

It was clear from the IPF maps in Figure 5, there is a subtle orientation change between the three maps with the microstructure rotating towards the <101> orientation direction with increasing depth. Close to the surface a strong Rotated Cube texture component is seen, which is the preferable deformation texture during upset processes. At position B, the Rotated Cube texture is still present but has shifted by approximately 15° towards Cube texture. In addition, Goss, which like Cube is a recrystallisation texture component [9], is seen to increase in intensity approaching the centre of the forging blank where these become the prominent textures, as shown by the ODFs in Figure 5. At the centre, additional intensities are seen relating to Copper (112)<111> and to a lesser extent Cube and Rotated Cube texture components. This evolution of texture from Rotated Cube towards Cube and Goss, particularly at the centre the forging, indicates a dominant dynamic recovery process close to the surface where the strain is minimum whilst dynamic recrystallisation dominants in areas of highest strain, *i.e.*, the centre of the forging blank.

3.3 The Effective Strain Effects on Microstructural Development after Heat treatment

3.3.1 Grain Size and Morphology

Figure 7 presents the effective strain simulation map as well as IPF//Forging Direction (FD) maps parallel to the forging direction at three depths throughout the forging. The evolution in grain shape is clearly seen from A to C. In area A where the strain is a minimum, a bimodal grain size is visible as are grains of spherical shape reminiscent of the as-HIP powder presented in Figure 3(b) indicating the retention of PPBs after heat treatment. It is also clear that with increased depth towards the centre of the blank, the grain shape becomes more equiaxed and a homogeneous microstructure is observed. Furthermore, the propensity for the

smaller grains decreased with depth and an increase in strain. The large variation in grain morphology along the forging axis (X-direction in Figure 7) indicates non-homogeneous grain growth during static recrystallisation, which is related to strain distribution generated during isothermal forging. This type of heterogeneous microstructure can be detrimental to the material as inconsistent grain morphology is likely to create a large variation in mechanical properties [28].

The grain size and shape variation across the forging direction and its correlation with strain distribution during forging is directly related to the presence of PPBs. Moreover, studies were able to relate these aspects with the processing route and suggested by excluding certain deformation processes, such as extrusion, prior to forging, a homogeneous microstructure is achievable at lower manufacturing costs [29–31]. However, despite numerous experimental trials, the majority of HIPed nickel-based superalloys suffer from the presence of PPBs which are detrimental to mechanical properties [32–38]. It is believed PPBs are generated by contamination of the powder surface via oxides, carbides and oxy-carbides which remain in the material after forging, and act to inhibit grain boundary migration [39,40]. The amounts of PPBs generated are entirely dependent on the amount of oxygen present during processing [37] and the level of carbon in the composition, and typically act as nucleation sites for stable Al_2O_3 and TiO_2 oxides along with brittle MC (Nb, Ti)C carbides within nickel-based superalloys [41,42]. The stable nature of these phases act to pin grain boundaries during growth resulting in grains of below average size compared to materials free of PPBs. It is possible to achieve decomposition of the primary MC carbides to M_{23}C_6 in alloys containing high Ti, low Nb, and, low Ta content via a two stage HIP process, and would aid to reduce the PPB networks. The reduction and elimination of PPBs has also been attempted through alteration of the material's oxygen or carbon content, and/or increasing the HIPing temperature [37,39,43]. Altering the levels of oxygen is particularly difficult during

atomisation due to the difficulties in improving vacuums during processing. Similarly with carbon, the amount present in modern nickel-based superalloys is already minimised to inhibit TCP formation whilst allowing carbide formation which proves beneficial in providing grain boundary pinning [44]. TCP formation may still be controlled with higher carbon contents but would require close control over the main TCP forming elements such as Cr, Mo and W whilst still achieving appropriate levels of γ' . Therefore the best possibility is increasing the HIP temperature which has been seen to promote grain boundary migration past PPBs with a compromise on levels of microstructure coarsening [7]. However, the alloy in the current study is part of a larger theme of research for which changes to powder processing and consolidation is deemed impractical for economic and time considerations. Therefore, the focus in the current study was optimising the forging parameters that may assist in breaking up the PPB network and in achieving a homogeneous microstructure in their presence.

3.3.2 Strain Distribution Effect on Recrystallisation

As reported in Section 3.3.1 the variation of strain rate and temperature across the forged materials produced different microstructure. Moreover, a large proportion of smaller grains ($<10\mu\text{m}$), which form a necklace structure around larger grains was found near the surface, see area A in Figure 7. This necklace structure was predominantly observed at the regions close to the forging surface corresponding to the areas of low effective strain. The presence of a necklace structure is not a new phenomenon in nickel alloys [45,46], and is indicative of varying levels of recrystallisation, both during dynamic (DRX) and static (SRX) recrystallisation processes. Typically DRX grains are small in size, in the region of $\sim 2\mu\text{m}$ diameter and were clearly visible in the as-forged alloy as shown in Figure 5. It is expected that during heat treatment of the forged material static recrystallisation would dominate the

nucleation and grain growth mechanism. However, observing the necklace microstructure in the heat treated condition implies an underlying relationship with dynamic recrystallisation and the levels of strain imparted during forging. Initial theories on the cause of DRX primarily focused on the levels of strain imparted during processing and its effect on deformation mechanisms. It is assumed that during isothermal forging the material undergoes super-plastic deformation, thus no significant levels of stored-strain was present in the material prior to heat treatment. Therefore, it was postulated that the level of strain imparted during hot deformation can cause DRX via strain-induced grain boundary migration [9]. Close to the surface (area A) where material flow is low, and thus strain is a minimum, recrystallisation kinetics would be sluggish in comparison to the centre of the forging blank (area C) where there are higher levels of strain to ensure widespread nucleation of recrystallised grains. This variation would then exacerbate during subsequent heat treatment processes resulting in the non-homogeneous microstructure. Figure 8(a) shows the distribution of grain area whilst 8(b) contains the average grain size of the bi-modal microstructure against effective strain. The grain area distribution shows a clear reduction in the volume of small grains sub $8.5\mu\text{m}$ at greater depths from the surface. From Figure 8(b) there exists a plateau up ~ 0.64 mm/mm where average grain size of the larger grains remains constant, followed by a transition to increasing grain size with strain to a maximum at the centre of the forging. From Figure 8 the crossover point between the increase in average large grain diameter and reduction in the smaller grain area occurs at a modelled strain in the range of 0.8 - 0.9 mm/mm effective strain. Using the relationship between the percentage of smaller (identified un-recrystallised) grains and strain, it was possible to use the Avrami equation, given in Equation 1, to predict the required levels of strain required for full recrystallisation [45,47].

$$X = 1 - \exp\left\{-\ln 2 \left[\frac{\bar{\epsilon}}{\epsilon_{0.5}}\right]^n\right\} \quad (\text{Eq. 1})$$

The recrystallised fraction, X , can be calculated through knowledge of the strain to 50% recrystallisation, $\epsilon_{0.5}$, the instantaneous strain, ϵ , and the Avrami exponent, n , which varies between 1.8 and 3.0 depending on the temperature range [45]. The use of the Avrami relationship has been used extensively within the literature and shows a good fit for modelling recrystallisation during hot deformation [48,49]. It was possible to calculate an approximate level of strain required for full recrystallisation using Equation 1, which for V207M was calculated to be 1.3 mm/mm. This increase in strain may be achieved by multiple methods but the most practical and efficient method would be alteration of the isothermal forging parameters to increase the level of upset during forging.

In the literature there is no agreement on whether dynamic recrystallisation or recovery is the dominating mechanism during isothermal forging. Previous work conducted on isothermal compression of this material [8] identified dynamic recovery as the dominant mechanism where little or no dynamic recrystallisation was observed at the compression temperatures and strains studied. The authors concluded that the material undergoes a process of continuous dislocation absorption in subgrain boundaries, resulting in the generation of HAGB and new grains termed as continuous dynamic recrystallisation [12,50] or dynamic recovery [51]. In contrary to the findings in [8], the results of this study fall in agreement with literature [12,51,52] where the dominating relaxation mechanism is dynamic recrystallisation. This conclusion is based on the levels of grain growth and texture evolution in the as-forged alloy observed here. This is expected in V207M nickel based superalloy alloy as it has low stacking fault energy and an ability to accumulate large amounts of dislocations that can provide the necessary energy for recrystallisation. However, further

validation of this result was needed through grain boundary characterisation and fibre texture analysis for the forging blanks as discussed below.

3.3.3 Strain Distribution Effect on Grain Boundary Characteristics

Grain boundary analysis was conducted on each of the 16 EBSD maps acquired in the current study to aid in further understanding of microstructural evolution during forging and heat treatment. Here, the aim was to establish a possible correlation between grain boundary migration and special boundary formation during forging which is closely related to deformation parameters. In the first instance, grain boundary angle is compared along the forging axis as seen in Figure 9. In general, immobile high angle grain boundaries ($> 15^\circ$) typically indicate a fully recrystallised grain where grain boundary junctions are typically at their lowest energy state (*i.e.* triple junction); whilst, low angle grain boundaries ($< 15^\circ$) are typically found in regions where a sub-grain microstructure exists. Furthermore, the formation of twin boundaries ($\Sigma 3$) is highly prevalent in FCC metallic alloys as in nickel-based alloys. The effect of twin boundaries on the mechanical properties is not fully understood however it is generally believed that they resist crack growth and can aid in inhibiting crack initiation [53]. EBSD data was used to identify the twin boundaries ($\Sigma 3$) and the twin boundaries fraction given as a percentage of the total boundaries within the given map area in this study. The twin boundary fraction versus depth from the forging surface is shown in Figure 9(b). Accompanying the graph is the corresponding 3 out of 16 EBSD-derived grain boundary angle and twin boundary maps for forged and heat treated conditions, see Figure 9(a). The high angle grain boundaries are shown in black and $\Sigma 3$ twins are shown in red (please refer to digital version). It is clear from Figures 9(a) and 9(b) that the fraction of $\Sigma 3$ twins increases with depth in both as-forged and heat treated conditions, with an overall increase of approximately 3% in the as-forged material and 16% after heat treatment. It was

evident that the twin boundary formation and growth correlated well with strain distribution within forged and heat-treated alloys. This also indicates strain accumulation in the dead-zone (area A) is not sufficient enough to produce high fraction of $\Sigma 3$, which is fundamental for mechanical property enhancement of the alloy. Therefore, greater strain was needed to achieve desired grain size and twin boundary volume fraction. The greater amount of strain was also required to obtain a higher volume fraction of recrystallisation texture components (*i.e.*, Cube and Goss) as indicated in the ODFs for area (C) in Figure 5 and 7. This texture change across the forging direction can be used to indicate dynamic and static recrystallisation in the forged and heat treated material respectively, and will be discussed in further detail in the next section.

3.3.4 Strain Distribution Effect on Texture Evolution

Further texture analysis was conducted on the overall local texture and fibre texture comparison between all 16 EBSD scanned areas including A, B and C. As reported earlier, the overall texture parallel to the forging axis is presented in Figures 5 and 7. The IPFs suggested a slight orientation change in as-forged condition whilst after heat treatment no significant preferred orientation was seen as is to be expected following static recrystallisation and grain growth during supersolvus heat treatment [52]. Comparison of the ODF plots showed an evolution from Rotated Cube (in area A) towards Cube and Goss (area C) in as-forged condition, shown in Figure 5. Following heat treatment, the ODF plots in Figure 7 showed the Rotated Cube and Goss texture components in area A as a result of the static recrystallisation. Whereas, in area C a high intensity $\sim 3^\circ$ away from ideal Cube was evident again indicating the occurrence of recrystallisation. It should be noted that the intensity of the texture remained almost constant throughout the forging and heat treatment but the texture components have changed dramatically.

Separate examination of the fibre texture allowed for texture comparisons to be correlated with a specific axis, which in this case is the forging direction (X-direction in Figure 5). In the current study, the focus was on the comparison of ($\langle 100 \rangle // \text{FD}$: Forging Direction), ($\langle 110 \rangle // \text{FD}$) and ($\langle 111 \rangle // \text{FD}$) fibre textures due to their relevance in FCC system deformation and recrystallisation mechanisms. The fibre texture maps taken at areas A, B and C are presented in Figures 10 and 11 for as-forged and heat treated condition respectively, with a deviation of 10° from ideal fibre orientation. The corresponding numerical results and comparison are presented in Figure 12. As can be seen in Figures 10 and 12, within the as-forged pancake the domination of $\langle 110 \rangle // \text{FD}$ fibre texture is approximately double that of the other two fibre textures. From the same figures, it is also clear that the large grains have $\langle 110 \rangle$ orientation preferences, whilst the small grains tend to have a $\langle 111 \rangle$ texture. In heat treated condition, the overall trend is similar to that of the as-forged material with a higher proportion of grains showing $\langle 110 \rangle$ fibre texture, greater than 12% texture fraction, followed by $\langle 100 \rangle$ and $\langle 111 \rangle$ fibres with texture fractions between 5-8%, shown in Figures 11 and 12. The texture distribution in the heat treated alloy is seen to be more random than that of the as-forged alloy where the exact correlation determination between texture and grain size was not possible, see Figure 11.

Figure 12 shows that in both forged and heat-treated alloys $\langle 110 \rangle$ and $\langle 100 \rangle$ fibres increases with depth, whilst $\langle 111 \rangle$ decreases. This is also in agreement with the ODF plots shown in Figures 5 and 7. From the ODFs in the same figures, the texture intensity in heat treated alloy is higher than in as-forged alloy which is a result of the additional thermal energy and time exposure for static recrystallisation and grain growth to occur during heat treatment. As can be seen in Figure 12a, $\langle 110 \rangle // \text{FD}$ fibre increased with increasing strain, *i.e.*, depth of the forging. It is also clear that its fraction in as-forged condition is higher than in heat-treated alloy. In general with low stacking fault energies, as in V207M and other nickel based

superalloys [54], slip is likely to occur on (111) planes along $\langle 110 \rangle$ direction in addition to twinning on the (111) planes along $\langle 112 \rangle$ direction. Thus, area A, *i.e.*, low strain, of the as-forged condition will have high intensity of Rotated Cube (001) $\langle 110 \rangle$ texture component. Furthermore, Goss is also on $\langle 110 \rangle //$ FD fibre. Therefore, the high fraction of $\langle 110 \rangle$ fibre in the as-forged alloy is related to high Rotated Cube which is the deformation texture component and Goss which indicates dynamic recrystallisation occurrence during forging, see the ODFs in Figure 5. It is also clear from Figure 12b, that $\langle 111 \rangle //$ FD fibre is decreasing with strain on both as-forged and heat treated alloys. This is expected in the heat-treated alloy for the texture component such as Copper (112) $\langle 111 \rangle$ which is typical deformation texture component on this fibre as static recrystallisation takes place. However, in forged condition the Copper texture component is known to be an unstable orientation and tends to twin easily during deformation [55–57] and thus $\langle 111 \rangle //$ FD fibre was also not strengthened during forging. The instability and easy twinning of Copper may also assist in increasing twin fraction with strain. As expected, the $\langle 100 \rangle //$ FD fibre increased with increasing strain, as shown in Figure 12(c). This is more related to enhancement of the Cube (001) $\langle 001 \rangle$ recrystallisation texture component during forging and heat treatment. However, this enhancement only occurred at higher strain areas (areas B and C) in the forged condition. Moreover, it appears that Goss (110) $\langle 001 \rangle$ texture formation assisted in increasing $\langle 001 \rangle$ fraction in the as-forged alloy than in heat-treated alloy. It is evident from the texture analyses that the degree of overall re-orientation during the forging depends on deformation levels. This in return is vital to estimate the exact strain required during forging to optimise the microstructure and texture to achieve the desired property of the alloy. The current study clearly demonstrates that the strain distribution within the forged and heat-treated material can greatly affect the microstructure and texture evolution including twin and grain boundary volume fraction.

4. Summary and Conclusions

The microstructure of experimental nickel-based superalloy V207M was examined by means of EBSD. Complimentary strain variation investigation was conducted in parallel using process modelling software Deform 2D. A complete characterisation of the materials microstructural evolution throughout a single forging was carried out with the aim of understanding the prominence of recrystallisation and recovery mechanism in achieving a homogeneous and not textured product. The following conclusions and observations are made base on the analysis:

1. Process modelling showed a dead zone to be present close to the forging surface with an effective depth of approximately 5mm at which the effective strain becomes radially uniform. The levels of strain varied throughout the forging from a minimum of 0.2mm/mm on the surface at the radial centre to a maximum of 1.15mm/mm at the centre. Investigation of the levels of adiabatic heating showed overall temperature increases to be minimal ($<3^{\circ}\text{C}$) and were thus considered negligible.
2. Investigation of the alloy powder showed a particle size distribution that was found to be consistent with that in the literature.
3. EBSD characterisation of V207M in as-HIPed condition revealed a bimodal grain size distribution and extensive prior particle boundary networks with little to no significant texture development.
4. V207M in as-forged condition showed both a coarsening of grain size with increased depth ($\approx 3\mu\text{m}$ increase) and an increase in the percentage of $\Sigma 3$ twin boundaries ($\approx 3\%$). Analysis of the texture showed an evolution from Rotated Cube at the surface to that of Goss and Cube at the centre. This analysis suggests that dynamic recovery is

dominant at the surface where strain is low and dynamic recrystallisation is dominant where levels of effective strain are highest.

5. Following solution heat treatment, V207M showed a necklace microstructure close to the surface where the propensity of the smaller grains reduced with increasing strain to a minimum at the forging centre. Close to the surface, grain shape remained spherical as a result of prior particle grain boundary effects on grain nucleation and growth mechanisms. Grain size and percentage of $\Sigma 3$ twins were both found to increase with increasing strain during static heat treatment to a maximum at the forging centre. The texture within the forging was one of primarily Rotated Cube and Goss at the surface evolving to that of a randomly orientated texture at the centre of the forging.
6. Correlation of the propensity of necklace grains after heat treatment and effective strain allowed for the estimation of minimum strain required to achieve 100% recrystallisation. It is suggested that a minimum strain of 1.3 mm/mm is required which is easily achieved during the isothermal forging process by increasing the amount of upset.

Acknowledgments

This work was financially supported by the EPSRC Rolls-Royce Strategic Partnership in Structural Metallic Systems for Gas Turbines (Grants EP/H500383/1(Research) and EP/H022309/1(Training)).

References

- [1] J.Y. Hwang, R. Banerjee, J. Tiley, R. Srinivasan, G.B. Viswanathan, H.L. Fraser, *Metall. Mater. Trans. A* 40 (2008) 24–35.
- [2] Y. Amouyal, Z. Mao, D.N. Seidman, *Acta Mater.* 58 (2010) 5898–5911.
- [3] S.T. Wlodek, R.D. Field, *TMS Superalloys 718, 625, 706 Var. Deriv.* (1994) 167–176.
- [4] L.A. Jackman, G.E. Maurer, S. Widge, *TMS Superalloys 718, 625, 706 Var. Deriv.* (1994) 153–166.
- [5] R.C. Reed, *The Superalloys Fundamentals and Applications*, 1st ed., Cambridge University Press, Cambridge, UK, 2006.
- [6] C.L. Qiu, M.M. Attallah, X.H. Wu, P. Andrews, *Mater. Sci. Eng. A* 564 (2013) 176–185.
- [7] G.E. Maurer, W. Castledine, F.A. Schweizer, S. Mancuso, *TMS Superalloys* (1996) 645–652.
- [8] P.M. Mignanelli, N.G. Jones, K.M. Perkins, M.C. Hardy, H.J. Stone, *Mater. Sci. Eng. A* 621 (2015) 265–271.
- [9] F.J. Humphreys, M. Hatherly, *Recrystallization and Related Annealing Phenomena*, 2nd ed., Elsevier, Oxford, 2004.
- [10] C.A. Dandre, S.M. Roberts, R.W. Evans, R.C. Reed, *Mater. Sci. Technol.* 16 (2000) 14–25.
- [11] X. Wang, G. Gottstein, *E. Br. Scr. Mater.* 46 (2002) 875–880.
- [12] H. Zhang, K. Zhang, S. Jiang, H. Zhou, C. Zhao, X. Yang, *J. Alloys Compd.* 623 (2015) 374–385.
- [13] S.L. Semiatin, K.E. McClary, a. D. Rollett, C.G. Roberts, E.J. Payton, F. Zhang, T.P. Gabb, *Metall. Mater. Trans. A* 44 (2013) 2778–2798.
- [14] M.A. Meyers, E.M. Lawrence, *Acta Metall.* 26 (1978) 951–962.
- [15] J.R. Cahoon, Q. Li, N.L. Richards, *Mater. Sci. Eng. A* 526 (2009) 56–61.
- [16] Q. Li, J.R. Cahoon, N.L. Richards, *Scr. Mater.* 55 (2006) 1155–1158.
- [17] M. Kumar, A.J. Schwartz, W.E. King, *Acta Mater.* 50 (2002) 2599–2612.

- [18] S. Mahajan, C.S. Pande, M.A. Imam, B.B. Rath, *Acta Mater.* 45 (1997) 2633–2638.
- [19] T. Watanabe, *J. Mater. Sci.* 46 (2011) 4095–4115.
- [20] P. Lin, G. Palumbo, U. Erb, K.T. Aust, *Scr. Metall. Mater.* 33 (1995) 1387–1392.
- [21] E.M. Lehockey, *J. Power Sources* 78 (1999) 79–83.
- [22] D.L. Olmsted, S.M. Foiles, E. a. Holm, *Acta Mater.* 57 (2009) 3694–3703.
- [23] D.. Brandon, *Acta Metall.* 14 (1966) 1479–1484.
- [24] M.C. Hardy, EP2562277B1, 2014.
- [25] J. Fluhrer, *DEFORM(TM) 2D Version 8.1 User's Manual*, Scientific Forming Technologies Corporation, Columbus, Ohio, 2015.
- [26] G.E. Totten, K. Funatani, L. Xie, *Handbook of Metallurgical Process Design*, Illustrate, CRC Press, 2006.
- [27] S.I. Oh, S.L. Semaitin, J.J. Jonas, *Metall. Trans. A* 23 (1992) 963–975.
- [28] J.R. May, M.C. Hardy, M.R. Bache, D.D. Kaylor, *Adv. Mater. Res.* 278 (2011) 265–270.
- [29] G. Raison, J.Y. Guédou, D. Guichard, J.M. Rongvaux, *Adv. Mater. Res.* 278 (2011) 277–282.
- [30] J.R. May, M.C. Hardy, M.R. Bache, D.D. Kaylor, *Adv. Mater. Res.* 278 (2011) 265–270.
- [31] J.E. Coyne, W.H. Coats, in: *High Temp. Alloy. Gas Turbines*, D. Reidel Publishing Company, London, 1982, pp. 839–852.
- [32] D.R. Chang, D.D. Krueger, R.A. Sprague, *TMS Superalloys* (1984) 245–273.
- [33] R.D. Kissinger, S.V. Nair, J.K. Tien, *TMS Superalloys* (1984) 285–294.
- [34] N.G. Ingesten, R. Warren, L. Winberg, *Adv. Mater. Manuf. Test. Information Anal. Cent.* (1982) 1013–1026.
- [35] M. Dahlen, N.G. Ingesten, H. Fishchmeister, *Mod. Dev. Powder Metall.* 14 (1981) 3–14.
- [36] J. Radavich, D. Furrer, M. Laboratories, N. Street, W. Lafayette, *TMS Superalloys* (2004) 381–390.
- [37] G.A. Rao, M. Srinivas, D.S. Sarma, *Mater. Sci. Eng. A* 435-436 (2006) 84–99.

- [38] G.A. Rao, M. Kumar, M. Srinivas, D.S. Sarma, *Mater. Sci. Eng. A* 355 (2003) 114–125.
- [39] D.L. Williams, *Powder Metall.* 2 (1977) 84–89.
- [40] G.A. Rao, M. Srinivas, D.S. Sarma, *Mater. Sci. Technol.* 20 (2004) 1161–1170.
- [41] G.A. Rao, M. Kumar, *Mater. Sci. Technol.* 13 (1997) 1027–1032.
- [42] R.G. Menzies, R.H. Bricknell, A.J. Craven, *Philos. Mag. A* 41 (1980) 493–508.
- [43] T.C. Lu, T.T. Nguyen, Y. Bienvenu, J.H. Davidson, O. Dugue, *High Temperature Alloys: Their Exploitable Potential*, Elsevier, London and New York, 1988.
- [44] C.S. Smith, *Trans. Metall. Soc. AIME* 175 47 (1948) 15–51.
- [45] G. Shen, S.L. Semiatin, R. Sivpuri, *Metall. Mater. Trans. A* 26 (1995) 1795–803.
- [46] Y. Wang, W.Z. Shao, L. Zhen, X.M. Zhang, *Mater. Sci. Eng. A* 486 (2008) 321–332.
- [47] M. Avrami, *J. Chem. Phys.* 8 (1940) 212–24.
- [48] K.G.F. Janssens, D. Raabe, E. Kozeschnik, M.A. Miodownik, B. Nestler, *Computational Materials Engineering: An Introduction to Microstructure Evolution*, Academic Press, 2010.
- [49] J.W. Cahn, *Acta Metall.* 4 (1956) 449–459.
- [50] S. Gourdet, F. Montheillet, *Mater. Sci. Eng. A* 283 (2000) 274–288.
- [51] S.L. Semiatin, D.S. Weaver, P.N. Fagin, M.G. Glavicic, R.L. Goetz, N.D. Frey, *Metall. Mater. Trans. A* 35 (2004) 679–693.
- [52] S.P. Coryell, K.O. Findley, M.C. Mataya, E. Brown, *Metall. Mater. Trans. A* 43 (2011) 633–649.
- [53] M.D. Sangid, T. Ezaz, H. Sehitoglu, I.M. Robertson, *Acta Mater.* 59 (2011) 283–296.
- [54] T. Leffers, R.K. Ray, *Prog. Mater. Sci.* 54 (2009) 351–396.
- [55] U.F. Kocks, C.N. Tome, H.R. Wenk, *Texture and Anisotropy: Preferred Orientation in Polycrystals and Their Effect on Materials Properties*, 1st ed., Cambridge University Press, Cambridge, UK, 1998.
- [56] I.J. Beyerlein, J.R. Mayeur, R.J. McCabe, S.J. Zheng, J.S. Carpenter, N. a. Mara, *Acta Mater.* 72 (2014) 137–147.

- [57] I.J. Beyerlein, N. a. Mara, D. Bhattacharyya, D.J. Alexander, C.T. Necker, *Int. J. Plast.* 27 (2011) 121–146.

Figure 1:- Schematic of forging section with area of EBSD investigation highlighted in red.

Figure 2:- Effective strain map using Deform 2D showing (a) Visual contours of strain distribution throughout forging, (b) variation of effective strain against depth.

Figure 3:- (a) Secondary electron image of pre-consolidated alloy powder with the vertical arrows highlighting satellite particles horizontal arrow showing melt impact films, (b) Secondary electron image of PPB boundary found in consolidated powder after electro-etching in 10% phosphoric acid.

Figure 4:- (a) Inverse Pole Figure (IPF) EBSD map of as-HIPed V207M, (b) Orientation Distribution Function (ODF) (section 0 and 45°) highlighting very weak texture.

Figure 5: (Top) Visual schematic of the Deform 2D variation of strain within the forging (on the plane of interest), (bottom) IPF maps and corresponding ODF plots showing texture in the as-forged condition.

Figure 6: Average grain size against depth of V207M in as-forged condition.

Figure 7: (Top) Visual schematic of the Deform 2D variation of strain within the forging (on the plane of interest), (bottom) IPF maps and corresponding ODF plots showing orientation and texture in heat treated condition.

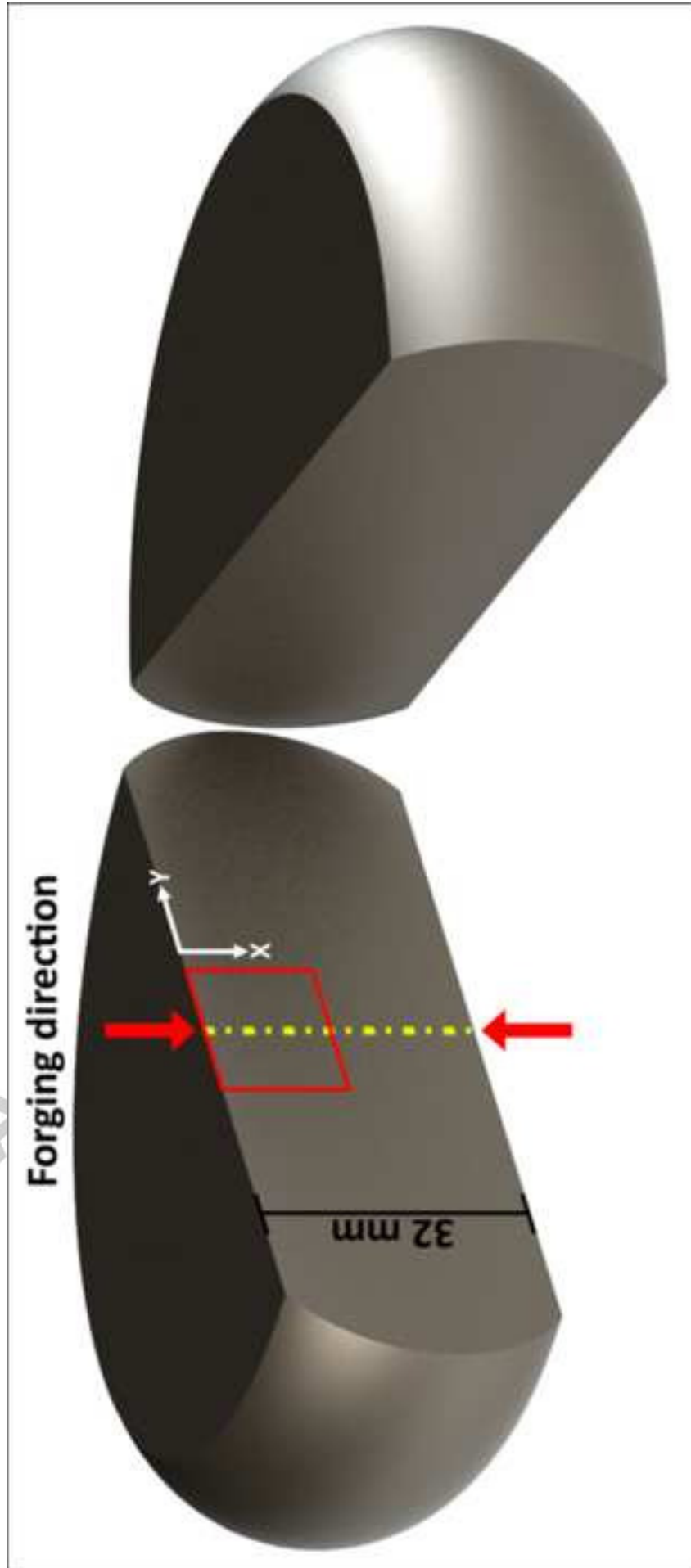
Figure 8: (a) Grain area distributions against depth showing a reduction in the area fraction of grain sub 8.5 μm . (b) Average grain size of the bi-modal microstructure.

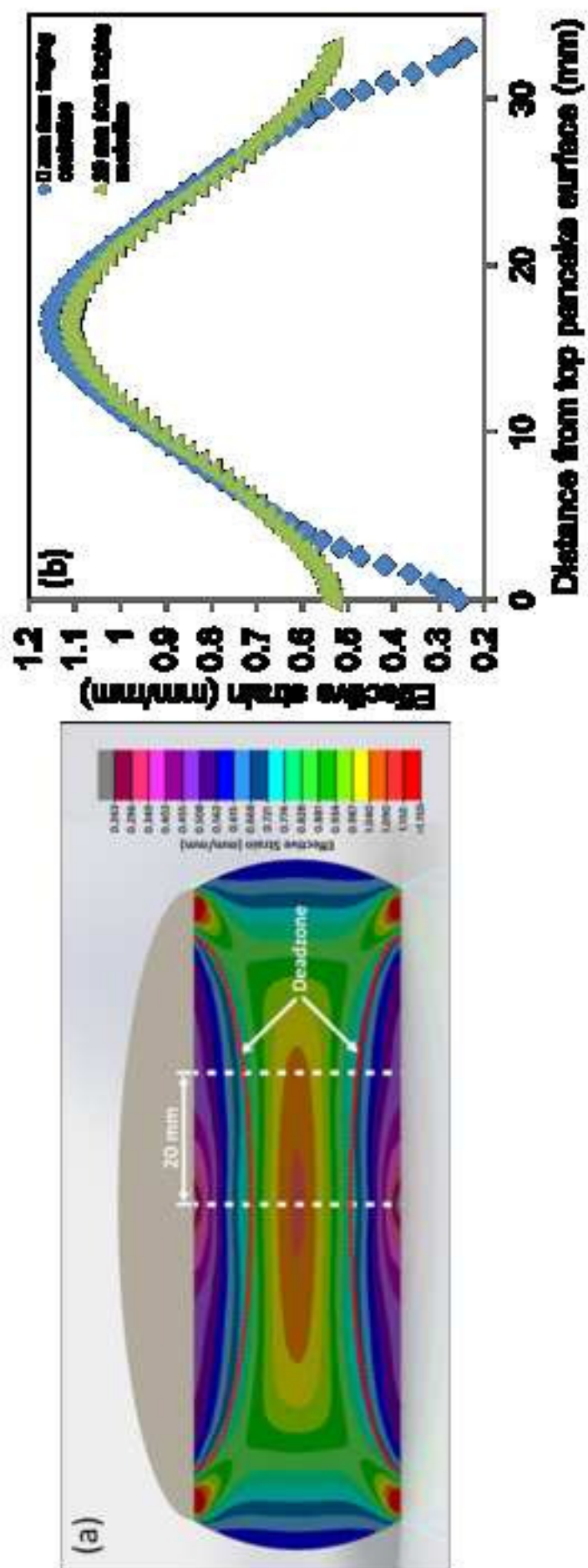
Figure 9: (a) EBSD grain boundary maps showing high angle grain boundaries in black and $\Sigma 3$ twin boundaries in red in as-forged (top) and heat treated (bottom) condition. (b) Scatter plot comparing twin boundary fraction against depth.

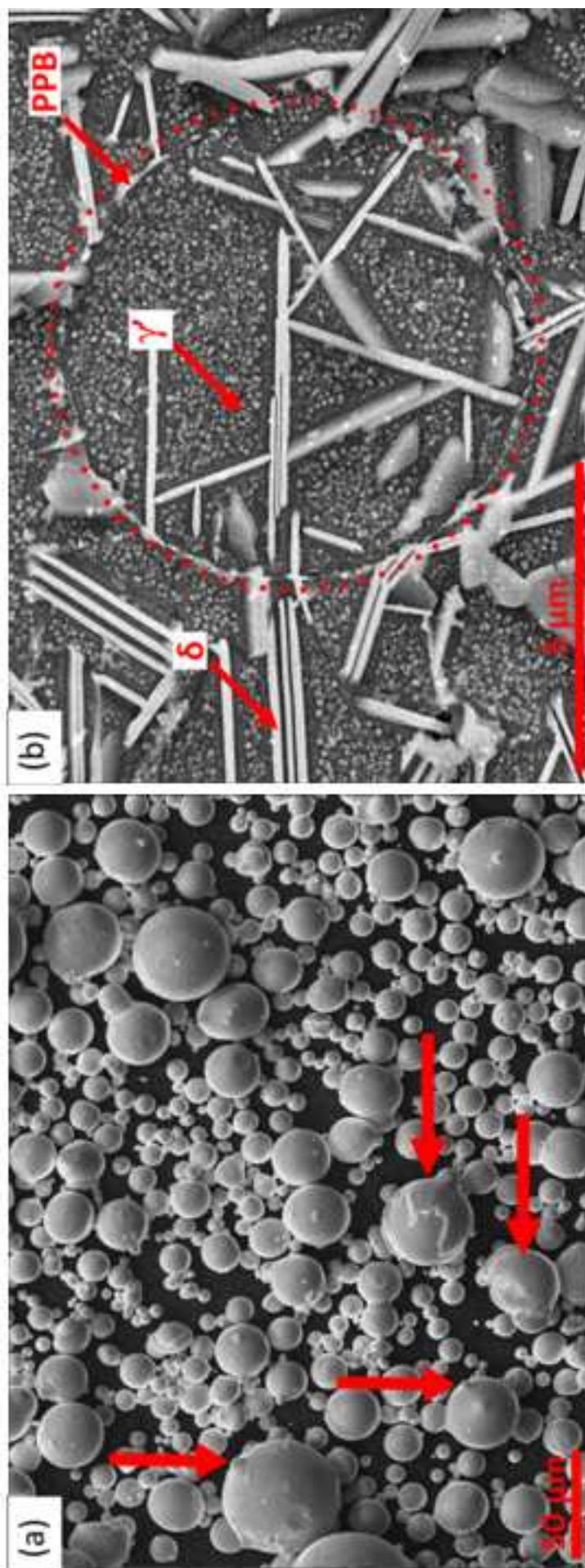
Figure 10: EBSD-derived $\langle 100 \rangle // \text{FD}$ fibre texture maps (top), $\langle 110 \rangle // \text{FD}$ (middle) and $\langle 111 \rangle // \text{FD}$ (bottom), for as-forged condition at three depths A, B and C.

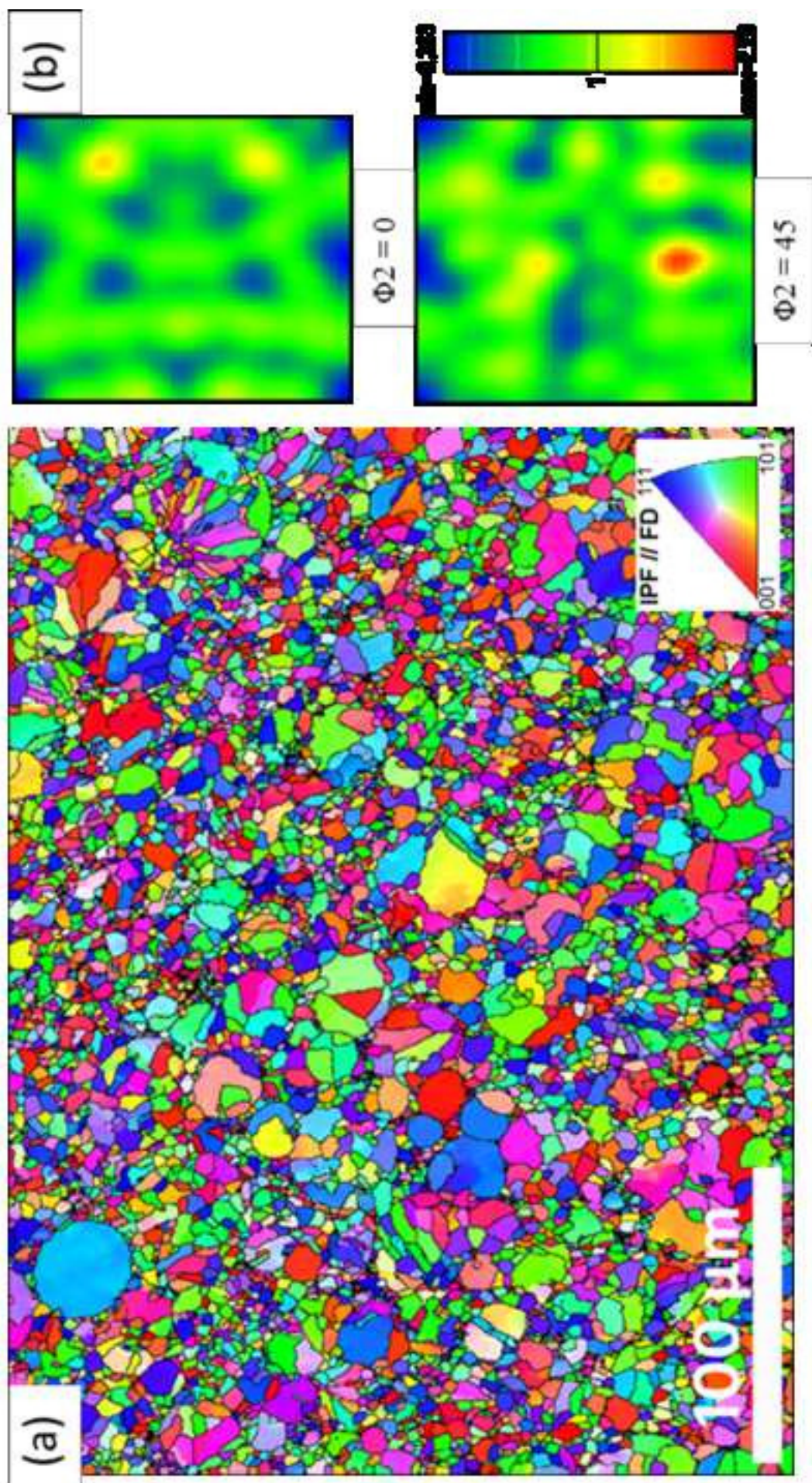
Figure 11: EBSD-derived $\langle 100 \rangle // \text{FD}$ fibre texture maps (top), $\langle 110 \rangle // \text{FD}$ (middle) and $\langle 111 \rangle // \text{FD}$ (bottom), after heat treatment at three depths A, B and C.

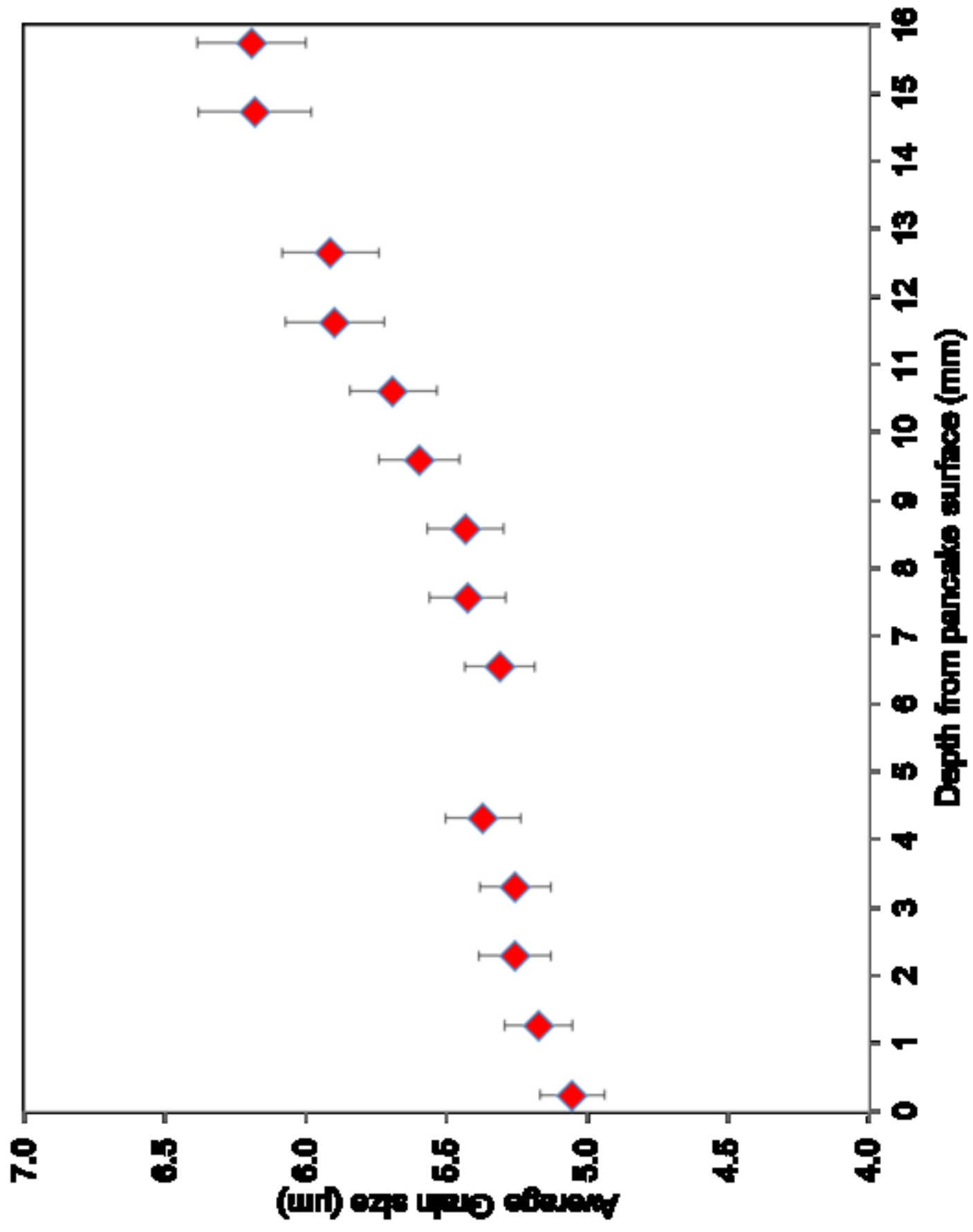
Figure 12: Graphical comparison of (a) $\langle 110 \rangle$, (b) $\langle 111 \rangle$ and (c) $\langle 100 \rangle$ fibre texture fraction against depth from pancake surface. All components use a maximum variation from ideal of 10°.











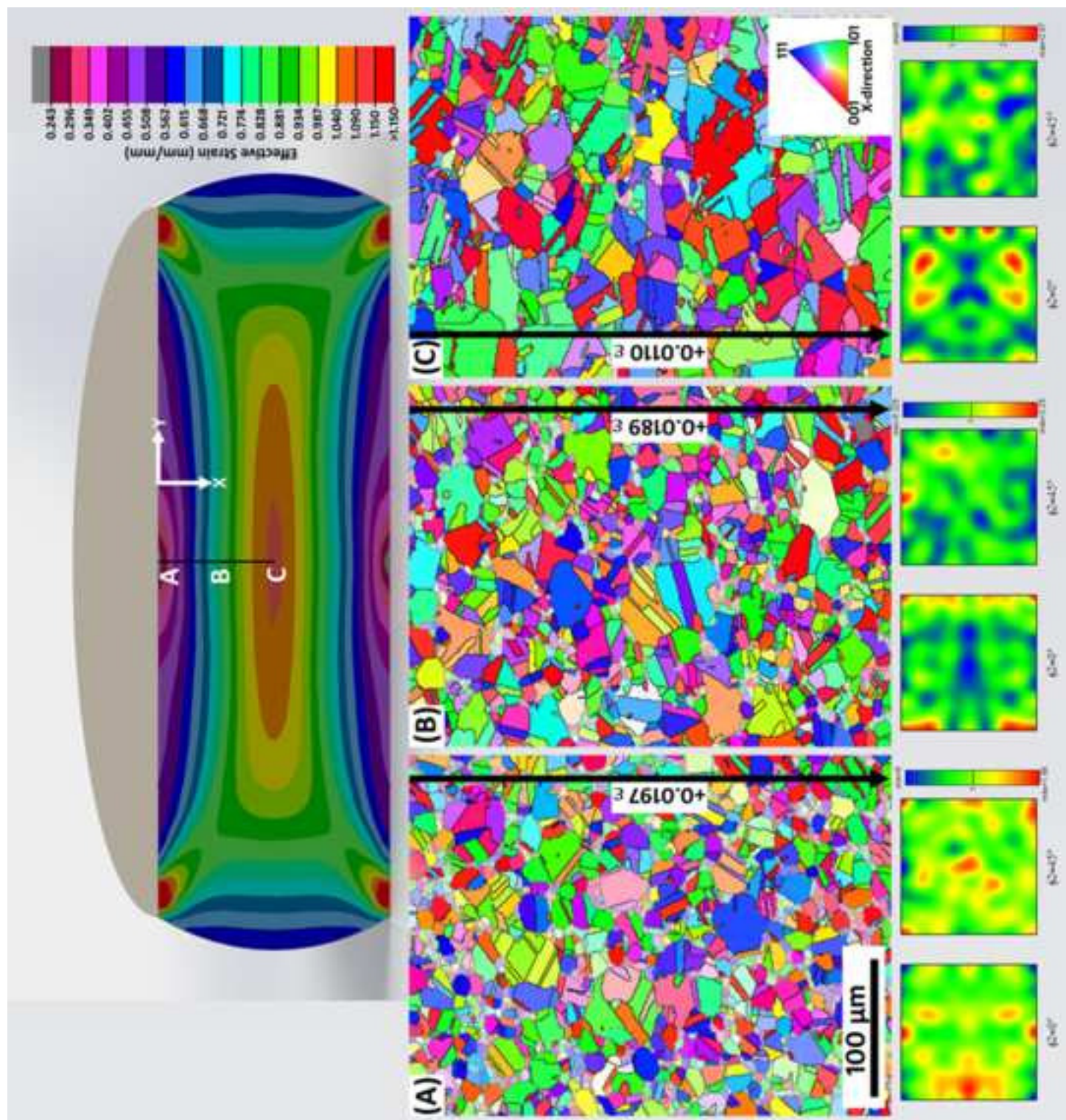


Figure_7 (2 column)

